Blinking Rolls: A Model for Three-Dimensional Chaotic Advection

P. Mullowney, K. Julien, J.D. Meiss*
Department of Applied Mathematics
University of Colorado
Boulder, CO 80309-0526

April 12, 2004

Abstract

We study a simple, nonautonomous, three-dimensional, incompressible flow corresponding to sequentially active two-dimensional rolls with distinct axes. A feature of the model is that an analytical map is obtained. We show that when the roll axes are orthogonal, motion is confined to two-dimensional topological spheres. The dynamics on each surface ranges from nearly regular to largely chaotic. We study the transport and mixing on each surface, and their dependence upon parameters in the system.

PACS 2003: 05.45.Ac, 45.20.Jj,47.52+j Keywords: chaotic advection, transport, volume-preserving mappings

1 Introduction

Fluid mixing corresponds to the transport of passive scalars by kinematic advection and their subsequent diffusive homogenization. Such phenomena are fundamentally important in many physical systems and engineering applications [1] and occur at a variety of scales ranging from the very small (micrometer scale) to the very large (planetary scales and beyond). For instance mixing in microchannels can be used to efficiently homogenize reagents in chemical reactions even when the flow is laminar [2]. Understanding transport for planetary scale flows is critical for climate modeling and pollution dispersion in atmospheric science [3] and eddy dynamics in oceanography [4]. Transport and mixing are also important in granular flows [5], population biology [6, 7], and reaction-diffusion systems [8].

The mixing of tracer particles in a fluid flow is due to a combination of stirring and diffusion. In an efficient mixing process, stirring rapidly transports tracer elements by kinematic advection throughout the domain. The associated stretching and folding of material lines and surfaces ultimately triggers diffusive processes that homogenize the tracers into a blended mixture. Originally, it was assumed that mixing was most important in the context of turbulent flows where both processes are evident. However, as is now well-known, effective mixing also occurs in laminar flows [9].

In three-dimensions, these problems are especially challenging from a theoretical standpoint. One of the earliest advances came with the work on the Arnold-Beltrami-Childress or "ABC"

*PM was supported by NSF VIGRE grant DMS-9810751 JDM was supported in part by NSF grant DMS-0202032, KJ was supported by an NSF grant OCE-0137347. We would like to thank H. E. Lomelí and P. Boyland for helpful discussions.

flow [10], an exact solution to the Euler equations. It was found that efficient stirring in three-dimensional incompressible flows can occur even for laminar and autonomous Eulerian velocity fields. Although the ABC flow is probably not physically observable, the crucial idea is that mixing can occur even in the simplest of flows in three-dimensions [1]. In the two-dimensional case, transport can also be achieved in laminar, time-dependent flows. One of the seminal models was developed by Aref, who coined the term "chaotic advection" [11]. His flow, called the "blinking vortex." is specifically designed to yield nonintegrable Lagrangian trajectories. This model can be interpreted as an idealized mixing protocol where passive tracers are successively captured by the velocity fields of vortical stirrers that are the analogues of turbulent eddies with finite lifetimes.

In §2 and §3, we generalize the blinking vortex model and construct a physically motivated, yet mathematically simple system with three-dimensional mixing. Our model, which we call "blinking rolls," replaces Aref's alternatively active vortices with alternatively active arrays of rolls aligned in different directions.

Though our mixing protocol is idealized, there is experimental evidence for the existence of similar flows. One such example is observed in Rayleigh-Bénard convection experiments for a binary mixture in a square cell with insulating sides. When the vertical temperature difference exceeds a threshold value, an instability leads to a sequence of temporally alternating, orthogonal convection rolls whose axes are parallel to the square boundaries [12]. It is observed that "the transition from one set of rolls to the other is very fast, followed by a relatively long period of domination by one of the rolls...the system lies most of the time in the roll patterns." Another example of roll-switching is the Küpper-Lortz instability for rotating convection in a pure fluid[13, 14, 15, 16, 17]. Rotation causes an instability that results in switching of the roll axes by roughly 60°. Theoretical and experimental studies have shown that the rolls switch with a characteristic frequency proportional to the relative temperature difference above threshold.

When the switching occurs much faster than the roll turnover time, it can be idealized as instantaneous. In this case, the flow can be viewed as a composition of maps corresponding to the action of each individual roll. For the incompressible case, this gives a composition of volume-preserving maps. Transport in volume-preserving maps was studied in pioneering work on a discretized ABC system [18, 19, 20, 21]. The onset of transport is closely related to the destruction of heteroclinic connections for codimension-one manifolds [22, 23]; a Melnikov method was developed to study the bifurcations in manifold crossings in [24, 25].

It is generally difficult to find models for three-dimensional flows that are both mathematically accessible and have effective transport. However, there is a small but growing link between mixing in experimental, three-dimensional flows and theoretical modeling based on chaotic advection. Shinbrot and his collaborators have studied the transient behavior of weakly buoyant tracers in a laminar flow within a cylindrical batch stirring device using using a traveling wave map with a buoyancy term [26]. In a similar though less symmetric device, a close link was found between the invariant regions of the flow visualized with a sheet laser and fluorescent dyes and the corresponding island chains of the Poincaré sections of a model [27, 28]. These examples reflect the growing evidence that mixing in three-dimensional flows can be effectively modeled via chaotic advection [1, 9]. This is crucial because it allows one to treat the flow as a low-dimensional dynamical system, and thus bring to bear the geometrical and qualitative tools of dynamical systems theory.

In this paper, we present a theoretical and computational analysis for the blinking roll model. In §2 the flow for a single roll is constructed and the equations of motion are solved to obtain an analytical time-T map. In §3 the flow with roll-switching is modeled by composing several of these maps. For the case that the roll axes are orthogonal, there is an invariant that constrains the motion to two-dimensional surfaces, §4. This system has a number of symmetries that simplify its analysis, §5. In §6, we use normal form expansions to understand behavior near a fixed point and

near roll boundaries. Numerical results are given in §7.

2 Blinking Rolls

Aref's blinking vortex flow corresponds to a two-dimensional, inviscid, incompressible, fluid in a circular domain of radius a [11]. A point vortex moves inside the bounding contour according to a stirring protocol $(x(t), y(t))$. The equations for a passive scalar in such a fluid are Hamiltonian, and if the vortex position is constant in either a fixed or steadily rotating coordinate system, then the flow is integrable. Otherwise the flow is typically nonintegrable.

The blinking vortex corresponds to a stirring protocol with period T. For the first half of the period, a vortex resides at $(b, 0)$ and for the remainder of the period a vortex resides at $(-b, 0)$ for some $b < a$. For simplicity it is assumed that there is an instantaneous transition between the flows associated with the finite-lifetime point vortices. This allows the equations of motion for each half period can be solved exactly, giving rise to the half period maps $F_1(x, y)$ and $F_2(x, y)$. The Lagrangian tracer dynamics is then governed by the full period map $f = F_2 \circ F_1$.

Two-dimensional transport can then be studied simply by iterating the map. The dynamics are governed by two dimensionless parameters $\mu = \frac{\Gamma T}{2\pi a^2}$, representing the vortex strength, and $\beta = \frac{b}{a}$, its relative radial position. If β is held fixed then for small enough μ, chaotic advection is localized and there is no global transport. As μ increases, the chaotic regions grow and the phase portrait becomes increasingly homogenized.

Here we will construct a three-dimensional model analogous to the blinking vortex system. The model consists of flows generated by a succession of two-dimensional "rolls" aligned in distinct directions that are applied for alternating time intervals. By "roll", we mean the circulating flow associated with a vortical tube where the vorticity vector and the tube axis are aligned. We do not consider drift along the roll axes. The flow is thus invariant along the roll axis and can be represented in terms of a stream function ψ with corresponding velocity field

$$\mathbf{v} = \nabla\psi(\mathbf{x}_\perp, t) \times \hat{\mathbf{e}}_\parallel \ , \tag{1}$$

where $\mathbf{e}_\parallel$ is the unit vector in the invariant direction. This generates motion in the $\mathbf{x}_\perp$-plane normal to $\mathbf{e}_\parallel$; if ψ is autonomous, this motion is also confined to a two dimensional surface defined by ψ constant. Any critical point of the stream function, i.e., a point where $\nabla\psi = 0$, corresponds to a stationary axis. Near such an axis the flow is rotational whenever the critical point is an extrema; the circulation near such an axis corresponds to a *roll*.

We will primarily study the case of an array of trigonometric rolls; when they are aligned in the x direction the stream function is given by

$$\psi = A\cos(y)\cos(z) \ . \tag{2}$$

This gives the velocity field

$$(\dot{x}, \dot{y}, \dot{z}) = \nabla\psi(y, z) \times \hat{\mathbf{e}}_x = (0, -A\cos(y)\sin(z), A\sin(y)\cos(z)) \ . \tag{3}$$

For this case, the line $(y, z) = (0, 0)$ is a roll axis (as are the axes $(m\pi, n\pi)$ for $m, n \in \mathbb{Z}$); nearby orbits lie on topological circles enclosing x-axis, see Fig. 1. These circles limit on a square as y and z approach $\pm\frac{\pi}{2}$. The line $(y, z) = (\frac{\pi}{2}, \frac{\pi}{2})$ and its translations by $(m\pi, n\pi)$ correspond to saddle equilibria. Indeed the square cylinder boundary of the set $\{|y|, |z| \leq \frac{\pi}{2}\}$ consists of the stable and unstable manifolds of the saddles, and bounds the roll surrounding the x-axis by heteroclinic

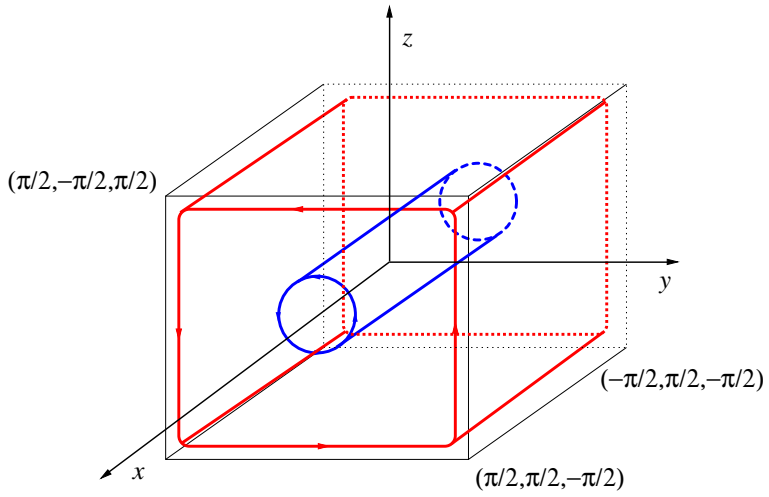

Figure 1: Flow of a two-dimensional roll, $\psi_1(y,z)$, with positive rotation about the x-axis.

connections. If $A > 0$, the direction of rotation for this roll is right-handed or *positive*. If we translate by π in a single direction, the direction of rotation becomes left-handed or *negative*.

A system of blinking rolls is obtained by alternatively switching between rolls aligned in different directions. A general mixing protocol can be implemented through a random specification of array lifetimes, amplitudes and phases. However, for simplicity and as a preliminary investigation we restrict ourselves to roll arrays that are confined to a periodic lattice.

For example, consider three different roll arrays defined by stream functions $\psi_i; i = 1, 2, 3$ and axes $\hat{\mathbf{e}}_i$ aligned with the unit vectors of a Cartesian coordinate system. Each roll has a corresponding velocity field v_i analogous to Eq. (3). Specifically, suppose that the roll ψ_3 is active for $0 \le t < T_3$, ψ_2 for $T_3 \le t < T_3 + T_2$, and ψ_1 for $T_3 + T_2 \le t < T_3 + T_2 + T_1$. We repeat this process periodically, so that the velocity field is time periodic with period $T = T_1 + T_2 + T_3$. While any one roll array, say ψ_i is active, then the motion is integrable, since ψ_i is constant and is confined to a plane of constant x_i. However, as each roll array acts successively, one would expect that the trajectories should explore a fully three-dimensional domain.

More generally, we could allow the array of rolls to have arbitrary, multiplicative time dependence, giving the general velocity field

$$\mathbf{v}(\mathbf{x}, t) = A(t)\nabla\psi_1 \times \hat{\mathbf{e}}_1 + B(t)\nabla\psi_2 \times \hat{\mathbf{e}}_2 + C(t)\nabla\psi_3 \times \hat{\mathbf{e}}_3 \; . \tag{4}$$

When $A(t)$, $B(t)$, and $C(t)$ are arbitrarily chosen, it is presumably impossible to solve explicitly for the flow. The blinking roll case corresponds to the choice of alternating step functions for $A(t)$, $B(t)$, and $C(t)$, see Fig. 2. If we fix the functions ψ_i, then this system has six parameters, the times, T_1, T_2, and T_3 and the amplitudes of the step functions A, B, and C. The amplitudes of the roll arrays are analagous to the eddy strength Γ in Aref's model.

Since only one roll array is active at any given time, if we can obtain an explicit solution for the flow of ψ_i, then we can construct an explicit time-t map during the period that one array is active. We denote the time T_i map for the stream function ψ_i by F_i:

$$F_i(x, y, z) = \Phi_{T_i}(x, y, z) \; , \quad \frac{d}{dt}\Phi_t = v_i(\Phi_t) \; , \quad \Phi_0 = id \; , \tag{5}$$

Here, the index i of F_i denotes the axis of rotation and the fixed direction under the map as well

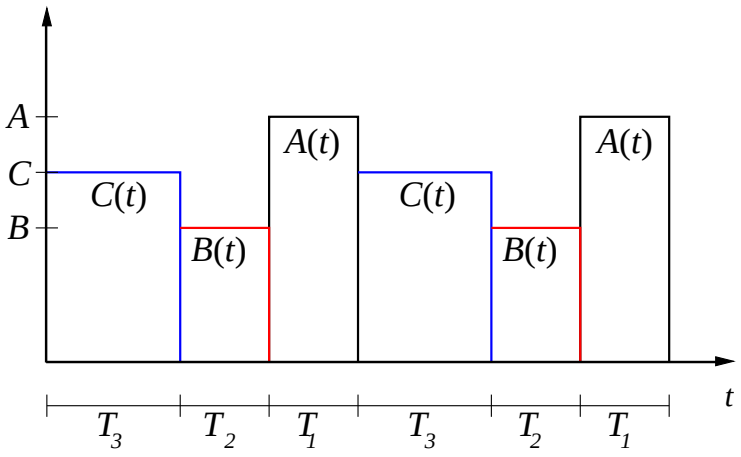

Figure 2: Step functions $A(t)$, $B(t)$, and $C(t)$.

as the time of activation T_i. The blinking roll map is the composition of these maps

$$(x', y', z') = F_1 \circ F_2 \circ F_3(x, y, z) \; . \tag{6}$$

Our next task is to obtain the the explicit solutions for the flow in the case of Eq. (2).

3 Blinking Roll Map

In this section we construct the 3D map for the velocity field Eq. (4) with rolls defined by Eq. (2) and amplitudes given by Fig. 2. We begin by solving for the flow of a single roll to obtain an explicit time-t map. Composition of the maps for each ψ_i gives the full 3D map Eq. (6).

The solution of the differential equations Eq. (3) can be easily obtained by noting that trajectories must satisfy $\frac{dy}{v_2} = \frac{dz}{v_3}$. The equations can be easily integrated in terms of Jacobi elliptic functions [29] to obtain the flow

$$\Phi_t \begin{pmatrix} x \\ y \\ z \end{pmatrix} = \begin{pmatrix} x \\ \sin^{-1}(k\mathrm{sn}(At - M(y,z), k)) \\ \sin^{-1}(k\mathrm{sn}(At + N(y,z), k)) \end{pmatrix} \; , \tag{7}$$

where the elliptic function modulus is

$$k = \sqrt{1 - \cos^2(y)\cos^2(z)} \; . \tag{8}$$

The functions $M(y,z)$ and $N(y,z)$ are defined by setting $t = 0$ to get the initial condition, e.g., $\sin y = -k\mathrm{sn}(M,k)$ and $\sin(z) = k\mathrm{sn}(N,k)$. Though solving for M and N appears to require inversion of the elliptic functions, a much simplified expression that does not require this can be obtained by expanding sn using the sum formula [29]

$$\mathrm{sn}(\alpha+\beta) = \frac{\mathrm{sn}(\alpha)\mathrm{cn}(\beta)\mathrm{dn}(\beta) + \mathrm{sn}(\beta)\mathrm{cn}(\alpha)\mathrm{dn}(\alpha)}{1 - k^2\mathrm{sn}^2(\alpha)\mathrm{sn}^2(\beta)} \; .$$

Note that the time t and amplitude A occur only in the combination At in Eq. (7). Thus if we rescale time by setting $T = At$, then we can eliminate the amplitude or roll strength parameter. As

we would like to consider the possibility that $A < 0$, giving negative roll rotation, we allow T to be negative. With this convention, the scaling is completely general. After scaling and simplification, the flow becomes:

$$\Phi_T \begin{pmatrix} x \\ y \\ z \end{pmatrix} = \begin{pmatrix} x \\ \sin^{-1}\left(\frac{\sin(y)\mathrm{cn}(T)\mathrm{dn}(T)-\mathrm{sn}(T)\sin(z)\cos^2(y)}{1-\sin^2(y)\mathrm{sn}^2(T)}\right) \\ \sin^{-1}\left(\frac{\sin(z)\mathrm{cn}(T)\mathrm{dn}(T)+\mathrm{sn}(T)\sin(y)\cos^2(z)}{1-\sin^2(z)\mathrm{sn}^2(T)}\right) \end{pmatrix} . \tag{9}$$

Eq. (9) depends explicitly on the initial condition and the modulus is still given by Eq. (8). Since typical numerical algorithms for Jacobi elliptic functions give sn, dn and cn simultaneously [30], having all three in the expression Eq. (9) has no additional numerical cost.

Since the amplitude has been scaled out, $\mathrm{sgn}(T)$ controls the direction of rotation of Φ_T, which of course satisfies the flow property $\Phi_{-T} = \Phi_T^{-1}$. Since cn and dn are even, and sn is odd, the only term that is affected by the switch in rotation direction is the second term in the numerator of each fraction in Eq. (9). By setting $T = T_1$, we get the time-T_1 map Eq. (5)

$$F_1(x, y, z) = \Phi_{T_1}(x, y, z)$$

from Eq. (9).

To obtain a three-dimensional map for blinking rolls, we consider the velocity field Eq. (4) with $A(t)$, $B(t)$, and $C(t)$ alternating, periodic step functions defined as in Fig. 2 and all three of the stream functions of analagous form to Eq. (2). All of the amplitudes can be removed by rescaling time; therefore without loss of generality we can set $A = B = C = 1$, leaving only the three parameters T_1, T_2, and T_3. Of course, the signs of these parameters represent the direction of rotation of the rolls. The maps F_2 and F_3 in Eq. (6) are obtained easily from Eq. (9) by permuting the variables appropriately.

4 Existence of an Invariant

Our numerically investigations for blinking orthogonal roll arrays indicate that three-dimensional mixing does not occur (see §7). Indeed, these investigations led to the discovery that the flow has an invariant for this case. This was unexpected since invariants are not common for volume-preserving flows and mappings that have no apparent symmetries (though some special examples have been constructed in [31]). As we see here, the flow of Eq. (4) does have a symmetry, although it is not immediately obvious.

Indeed, there is an invariant for the case of three rolls if we choose the stream functions to have the separable forms

$$\psi_1 = g(y)h(z) , \quad \psi_2 = f(x)h(z) , \quad \psi_3 = f(x)g(y) . \tag{10}$$

In this case it is easy to see that for *arbitrary* amplitude functions $A(t), B(t)$, and $C(t)$, the function

$$J = f(x)g(y)h(z) \tag{11}$$

is an invariant for the flow. To see this in a pedestrian way, one need only show that

$$\frac{dJ}{dt} = \nabla J(\mathbf{x}) \cdot \mathbf{v}(\mathbf{x}, t) = 0 , \tag{12}$$

as is easy to demonstrate using Eq. (4).

More generally if $\nabla J \neq 0$, then Eq. (12) implies there exists a vector field $\mathbf{E}(\mathbf{x}, t)$ such that [32]

$$\mathbf{v}(\mathbf{x}, t) = \nabla J \times \mathbf{E}(\mathbf{x}, t) \; . \tag{13}$$

This flow is volume-preserving providing

$$\nabla \cdot \mathbf{v} = -\nabla J \cdot (\nabla \times \mathbf{E}(\mathbf{x}, t)) = 0 \; .$$

One solution of this is $\mathbf{E} = \nabla \varphi(\mathbf{x}, t)$.[1] If φ were time-independent, then it would also be an invariant, and the flow would be integrable. However, if the velocity depends upon time, there need not be a second invariant (as we will see in §7). For example, the field $\mathbf{E} = (E_x(x,t), E_y(y,t), E_z(z,t))$ is curl-free, and the resulting velocity field is a superposition of the roll-like terms $v_i = E_{x_i}(x_i, t) \nabla J \times \hat{\mathbf{e}}_i$. The velocity of Eq. (4) with the separable stream functions Eq. (10) is obtained by choosing a suitable J of the form Eq. (11) and

$$\mathbf{E} = \left(\frac{A(t)}{f(x)}, \frac{B(t)}{g(y)}, \frac{C(t)}{h(z)} \right) \; .$$

When written in this way, the invariance of J is rather obvious from Eq. (13).

For cosine rolls, we choose $f = g = h = \cos$, and the invariant is

$$J = \cos(x) \cos(y) \cos(z) \; . \tag{14}$$

The invariant surfaces, shown in Fig. 3, are nested topological spheres centered at the origin that become cube-like near the boundary given by $x = \pm\frac{\pi}{2}$, $y = \pm\frac{\pi}{2}$, or $z = \pm\frac{\pi}{2}$. Since there is an invariant, the trajectories are confined to these surfaces, and there will be no three-dimensional mixing. However, the flow still exhibits considerable complexity as we will see in §7.

5 Symmetries

The trigonometric roll Eq. (3) is periodic with period 2π and is odd under translation by π in y or z. This implies that the fundamental cube for the three-dimensional flow Eq. (4) is divided into eight cells with alternating rotation directions; the case that all $T_i > 0$ is shown in Fig. 4. The $\pm$ signs in the figure indicate the directions of right (left) handed rotation for each roll, respectively.

The flows in the eight cells are equivalent, as we can see by considering symmetries of the vector field. A map R is a symmetry of $\mathbf{v}$ if $DR^{-1} \circ \mathbf{v} \circ R = \mathbf{v}$. It is easy to see that the velocity for trigonometric rolls has the four symmetries

$$\begin{aligned} R(x,y,z) &= (-x,-y,-z) & P_1(x,y,z) &= (x+\pi,-y,-z) \\ P_2(x,y,z) &= (-x,y+\pi,-z) & P_3(x,y,z) &= (-x,-y,z+\pi) \end{aligned} \tag{15}$$

corresponding to a reflection through the origin (R), and translations of x_i by π with a reflection through a perpendicular plane (P_i). There are also a symmetries from 2π translations. The group of symmetries generated by Eq. (15) is Abelian and has sixteen elements. Taking into account the 2π periodicity, this group of symmetries maps the flow in the cell $|x|, |y|, |z| < \frac{\pi}{2}$ onto the other seven cells.

Note that there are two possible structures; one corresponding to the choice of all positive times T_i as shown in Fig. 4, and the other to all negative times, created by flipping the signs of each roll.

[1] More generally, $\mathbf{E}$ need not be curl-free—its curl must only be tangent to the surfaces of constant J.

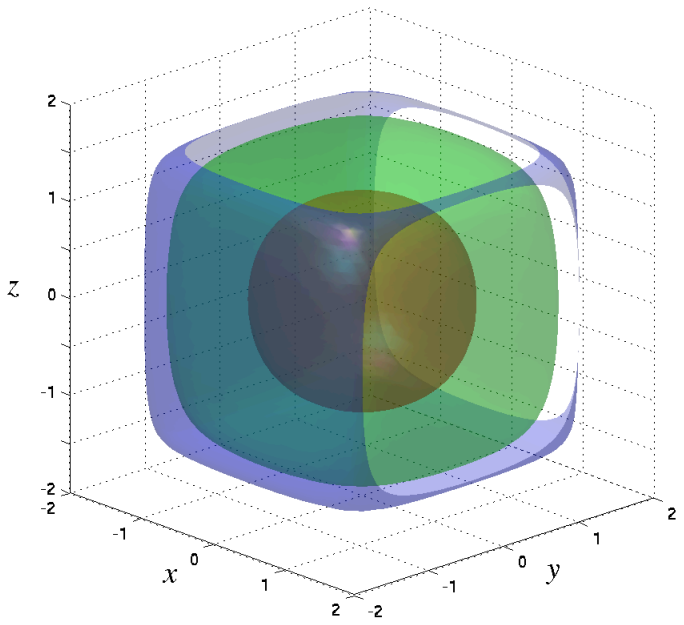

Figure 3: Three level sets of the invariant Eq. (14). The gaps in the outer surface are used to illustrate the concentric structure of the level sets.

There does not seem to be any way to map $(+++)$ onto $(---)$. To see this, let $t \to -t$. Then, in order for the veloctiy field Eq. (4) to remain unchanged under time reversal transformations, the functions $A(t)$, $B(t)$, and $C(t)$ must be odd. This contradicts the definitions given in §2. Thus there are two signed cases that should be considered to obtain all possible behaviors.

A numerical study of the behavior depending upon all three parameters is tedious. In §7 we will primarily study a two roll map

$$F_{ij} = F_i \circ F_j \ , \tag{16}$$

for some choice of i and j. We will now show that without loss of generality, we can restrict consideration to a single choice of the indices i, j, say $i = 1$ and $j = 3$, and to the case that $T_1 > T_3 > 0$. We do this by exploiting some of the obvious symmetries of Eq. (16).

It is trivial to show conjugacies between Eq. (16) and three other maps: $F_i^{-1} \circ F_j^{-1}$, $F_i \circ F_j^{-1}$, and $F_i^{-1} \circ F_j$. This is accomplished by defining S_i and H_i (for $i = 1, 2, 3$) as follows:

$$S_1(x, y, z) = (x, -z, y) \ , \qquad\qquad H_1(x, y, z) = (-x, y, z) \ ,$$

plus cyclic permutations. Here the map S_i is a positive rotation by $\frac{\pi}{2}$ about the i^{th} axis and H_i is a reflection about the plane perpendicular to the i^{th} axis. Thus $H_i^2 = id$ and $H_i \circ H_j = H_j \circ H_i$. A simple calculation then shows that

$$S_i \circ F_i \circ S_i^{-1} = F_i \ , \qquad\qquad H_i \circ F_i \circ H_i = F_i \ .$$

Applying the ith rotation to the jth map gives

$$S_1^{-1} \circ F_2 \circ S_1 = S_2 \circ F_1 \circ S_2^{-1} = F_3^{-1} \ ,$$
$$S_1 \circ F_2 \circ S_1^{-1} = S_2^{-1} \circ F_1 \circ S_2 = F_3 \ ,$$

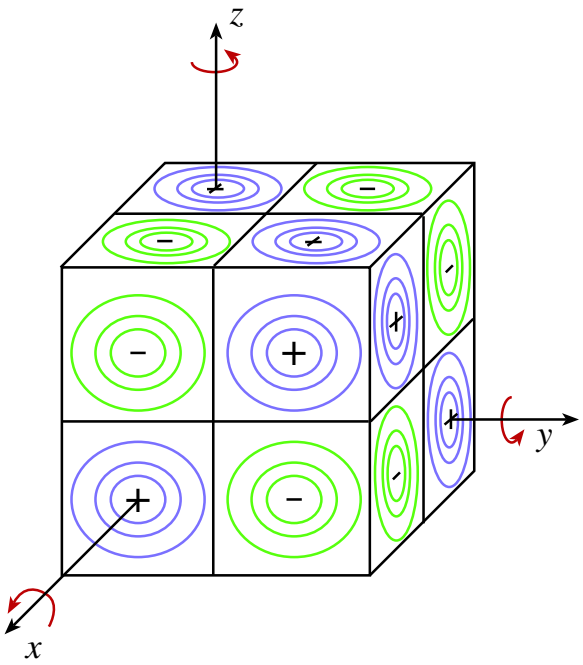

Figure 4: Fundamental cube ($-\frac{\pi}{2} < x, y, z < \frac{3\pi}{2}$) for cosine rolls when $T_i > 0$. The + sign stands for a right-handed rotation and the − for a left-handed.

and all cyclic permutations. Similarly for the reflection

$$H_1 \circ F_2 \circ H_1 = F_2^{-1} \ , \qquad\qquad H_1 \circ F_3 \circ H_1 = F_3^{-1} \ ,$$

and all cyclic permutations. Using these we obtain

$$H_k \circ F_i \circ F_j \circ H_k = \begin{cases} F_i^{-1} \circ F_j & \text{if } k = j \neq i \\ F_i \circ F_j^{-1} & \text{if } k = i \neq j \\ F_i^{-1} \circ F_j^{-1} & \text{if } k \neq i \text{ and } k \neq j \end{cases} . \tag{17}$$

From this we conclude that once a particular i and j are picked, the direction of rotation for each component is irrelevant because the maps are all conjugate to one another.

We next show that maps with different choices of i and j are conjugate. As the axes can be mapped onto each other by rotations, we consider

$$S_k^{-1} \circ F_i(T_i) \circ F_j(T_j) \circ S_k \quad \text{for } \ i \neq j$$

which switches one or both axes of rotation depending upon the choice of k. Here we have explicitly put in the parameter T, since it will be important below. First, for the case $k = i$,

$$S_i^{-1} \circ F_i(T_i) \circ F_j(T_j) \circ S_i = \begin{cases} F_i(T_i) \circ F_{i-2}(T_j) & \text{if } \ j = i-1 \\ F_i(T_i) \circ F_{i+2}^{-1}(T_j) & \text{if } \ j = i+1 \end{cases} ,$$

where the indices are understood modulus 3. Next, if $k = j$ then

$$S_j^{-1} \circ F_i(T_i) \circ F_j(T_j) \circ S_j = \begin{cases} F_{j-2}(T_i) \circ F_j(T_j) & \text{if } \ i = j-1 \\ F_{j+2}^{-1}(T_i) \circ F_j(T_j) & \text{if } \ i = j+1 \end{cases} .$$

Combining these relations with Eq. (17), shows that maps with all possible choices of different axes and different rotation directions are conjugate to one another. The critical point is that the first roll must be active for time T_j, and the second roll must be active for T_i as stated originally in Eq. (16).

Finally for the case if $k \neq j \neq i$ we find:

$$\begin{aligned} S_k^{-1} \circ F_i(T_i) \circ F_j(T_j) \circ S_k &= \begin{cases} F_j^{-1}(T_i) \circ F_i(T_j) & \text{if} \quad k = j+1 \\ F_j(T_i) \circ F_i^{-1}(T_j) & \text{if} \quad k = j-1 \end{cases} \\ &\cong F_j^{-1}(T_i) \circ F_i^{-1}(T_j) \quad \text{by Eq. (17)} \\ &= (F_i(T_j) \circ F_j(T_i))^{-1} \end{aligned}$$

Thus F_{ij} is conjugate to its inverse with time parameters swapped. Since, orbits are mapped to orbits under inversion (and the maps are bijections), the phase portrait of the dynamics of the map $F_i(T_i) \circ F_j(T_j)$ will appear conjugate to that of $F_i(T_j) \circ F_i(T_i)$.

In conclusion, for the two roll map Eq. (16) the direction of rotation is irrelevant so that only positive times need to be considered. Moreover, the choice of particular axes of rotation is irrelevant (so long as they're different). Finally, only the case $T_i > T_j$ need be studied, because the original map is conjugate to its inverse with time parameters swapped.

6 Normal Forms

The dynamics of Eq. (6) near the origin and on the boundary of the fundamental cube are relatively simple. In this section we use a normal form expansion near the origin to explore the effect of the nonlinear terms on the elliptic fixed point. We will show that when the map has an invariant, the dynamics near the origin are especially simple: the orbits of the normal form lie on invariant circles. To study the motion on the boundary of the fundamental cube, we use the fact that Eq. (9) reduces to a pair of one-dimensional maps analogous to shear flow on appropriate pieces of the boundary ($y = \pm\frac{\pi}{2}$ and/or $z = \pm\frac{\pi}{2}$). This implies that for Eq. (6), the dynamics on the boundary are relatively simple.

6.1 Motion Near the Origin

The asymptotic behavior of a map near a fixed point a map can be profitably studied using normal forms [33]. Normal forms were introduced by Birkhoff for the area-preserving case [34]; similar forms for volume-preserving mappings near a fixed point have been studied by Bazzani [35, 36]. The analysis in these papers excludes the case that the fixed point is linearly stable, which is of interest to us, so we explain some of the details of the calculation here.

The linear behavior of Eq. (6) near the origin is governed by the Jacobian matrix

$$DF(0) = DF_1(0)\, DF_2(0)\, DF_30) \; .$$

It is straightforward to see that the Jacobian of Eq. (9) at the origin is

$$D\Phi_T(0) = \begin{pmatrix} 1 & 0 & 0 \\ 0 & \cos(T) & -\sin(T) \\ 0 & \sin(T) & \cos(T) \end{pmatrix} \; .$$

This implies that each DF_i is a rotation about the axis $\hat{e_i}$ by angle T_i, and therefore that $DF(0) \in SO(3)$. It is well known that any special orthogonal matrix is a rotation about some axis; therefore

$DF(0)$ must have a complex conjugate pair of eigenvalues with modulus one

$$\lambda_{1,2} = e^{\pm 2\pi i\omega}$$

and one unit eigenvalue $\lambda_3 = 1$, with eigenvector v_3 corresponding to the rotation axis. In our case, we find that

$$\cos(2\pi\omega) = \frac{1}{2}(\sin T_1 \sin T_2 \sin T_3 + \cos T_1 \cos T_2 + \cos T_2 \cos T_3 + \cos T_3 \cos T_1 - 1) \ .$$

Thus $DF(0)$ is a rotation about the axis v_3 with angle $2\pi\omega$.

The first step in a normal form transformation is to diagonalize the linear system. We can diagonalize $DF(0)$ using a complex coordinate transformation $(x, y, z) \to (u, \bar{u}, w)$ where w represents the coordinate along the eigenvector v_3, u is the complex coordinate in the perpendicular plane, and $\bar{u}$ is the complex conjugate. The linearization then becomes

$$(u', \bar{u}', w') = \Lambda(u, \bar{u}, w) \ , \quad \Lambda = \begin{pmatrix} e^{2\pi i\omega} & 0 & 0 \\ 0 & e^{-2\pi i\omega} & 0 \\ 0 & 0 & 1 \end{pmatrix} \ .$$

we denote the map in the new coordinates $\mathbf{u} = (u, \bar{u}, w)$ by $\mathcal{F}$, so that $D\mathcal{F}(0) = \Lambda$. Expand $\mathcal{F}$ in a power series expansion of the form

$$\mathcal{F}(\mathbf{u}) = \Lambda(\mathbf{u} + \mathcal{F}^{(k)}(\mathbf{u}) + \mathcal{F}^{(k+1)}(\mathbf{u}) + \cdots) \ ,$$

where $\mathcal{F}^{(k)}$ is a term that is homogeneous of degree $k > 1$ in the variables $\mathbf{u}$, i.e.,

$$\mathcal{F}^{(k)} = \sum_{m+n+p=k} a_{m,n,p} u^m \, \bar{u}^n \, w^p \ , \tag{18}$$

with $m, n, p \in \mathbb{Z}_+$, and complex coefficients $a_{m,n,p}$. Since the original map is real, $\bar{u}$ is the complex conjugate of u, and thus $\bar{a}_{m,n,p} = a_{n,m.p}$.

The normal form for $\mathcal{F}$ is a "simpler" map $\mathcal{G}$ that is conjugate to $\mathcal{F}$,

$$\mathcal{G}(h(\mathbf{u})) = h(\mathcal{F}(\mathbf{u})) \ , \tag{19}$$

by a near identity transformation h. As usual we expand the conjugacy h and the new map in power series, and at each order use h to remove as many terms in $\mathcal{G}$ as possible. At order k all terms in $\mathcal{F}^{(k)}$ can be removed except those that are "resonant", i.e. those terms in the q^{th} component of Eq. (18) for which the integers satisfy

$$\lambda_1^m \lambda_2^n \lambda_3^p = e^{2\pi i(m-n)\omega} = \lambda_q \tag{20}$$

For each ω, we denote the solutions of Eq. (20) by R, and the normal form becomes

$$\mathcal{G} = \Lambda(\mathbf{u} + \mathcal{F}_R^{(k)}(\mathbf{u}) + \ldots)$$

where $\mathcal{F}_R^{(k)}$ denotes those terms in Eq. (18) for which m, n, p are in R.

When ω is irrational, Eq. (20) shows that resonances occur when

$$\begin{array}{ll} m = n + 1 \ , & \text{for } q = 1 \ , \\ m = n - 1 \ , & \text{for } q = 2 \ , \\ m = n \ , & \text{for } q = 3 \ . \end{array}$$

Since we can eliminate the non-resonant terms to all orders, the normal form becomes

$$u' = e^{2\pi i\omega} u \left(1 + \sum_{n,p\geq 0} \alpha_{2n,p} |u|^{2n} w^p \right)$$
$$w' = w \left(1 + \sum_{n,p\geq 0} \beta_{2n,p-1} |u|^{2n} w^{p-1} \right) , \tag{21}$$

where $\beta_{n,p}$ is real and $\alpha_{0,0} = \beta_{0,0} = 0$, since the corrections must be nonlinear. As is true for general normal form theory, Eq. (21) commutes with the group generated by Λ; since we assumed ω is irrational it commutes with arbitrary rotations about the w-axis. Note that the series Eq. (21) is not guaranteed to converge, even in some neighborhood of the origin, and thus must be viewed only in an asymptotic sense.

As demonstrated in §5, the map Eq. (6) has reflection symmetry through the origin. In this case, the normal form will exhibit the same symmetry, and therefore all even order terms drop out of the expansion so that

$$\alpha_{2n,2p+1} = \beta_{2n,2p+1} = 0 .$$

In addition, if F is volume preserving, then we can choose h so that it also preserves volume, and therefore the normal form will as well;

$$du' \wedge d\bar{u}' \wedge dw' = du \wedge d\bar{u} \wedge dw .$$

This places restrictions on the coefficients of Eq. (21). To cubic order, we find

$$\beta_{2,0} = -4\mathrm{Re}(\alpha_{2,0}) \qquad \beta_{0,2} = -\frac{2}{3}\mathrm{Re}(\alpha_{0,2}) . \tag{22}$$

Now, we can analyze basic phenomena of the normal form. Letting $u = \rho e^{2\pi i\theta}$, we can rewrite Eq. (21) to obtain the real map

$$\rho' = \rho(1 - \frac{1}{4}\beta_{2,0}\rho^2 - \frac{3}{2}\beta_{0,2}w^2 + O(3))$$
$$\theta' = \theta + \omega + \mathrm{Im}(\alpha_{2,0})\rho^2 + \mathrm{Im}(\alpha_{0,2})w^2 + O(3)$$
$$w' = w(1 + \beta_{2,0}\rho^2 + \beta_{0,2}w^2 + O(3))$$

Thus the origin is a nonhyperbolic fixed point. To all orders, the w-axis ($\rho = 0$) and the equatorial plane $w = 0$ are invariant. The plane $w = 0$ is locally an (un)stable manifold of the origin when $\beta_{2,0} > 0$ (< 0), and the w-axis is locally (un)stable when $\beta_{0,2} < 0$ (> 0). There are additional unstable manifolds along the lines $\rho = sw$ when $s^2 = -2\frac{\beta_{0,2}}{\beta_{2,0}} > 0$, and these are (un)stable manifolds when $\beta_{0,2} > 0 (< 0)$. An example is shown in Fig. 5.

Note that when there is an invariant whose surfaces are topological spheres about the origin (as is the case for Eq. (6)) none of the invariant axes can be attracting or repelling. Thus the only normal form that corresponds to this case is one in which *every* resonant coefficient has real part zero. Thus the normal form for Eq. (6) with irrational ω fixes ρ and w, and every orbit near the origin lies on an invariant circle. As we will see, this corresponds well with the numerical observations of the dynamics of Eq. (6) in §7.

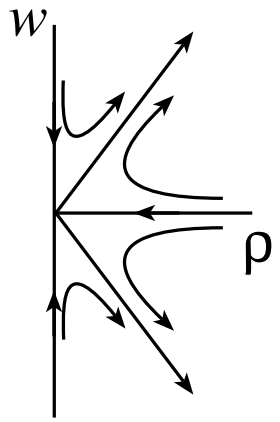

Figure 5: Dynamics of the normal form in the (ρ, w) plane for $\beta_{2,0} > 0$ and $\beta_{0,2} < 0$.

6.2 Motion on the boundary cube

The single roll flow, Eq. (9) preserves the boundaries of the fundamental cube, the surfaces where x, y, or z are $\pm\frac{\pi}{2}$. Recall from §2, that the line $(y, z) = (\frac{\pi}{2}, \frac{\pi}{2})$ and its translations by $(m\pi, n\pi)$ consist of saddle equilibria of Φ_T. The four faces corresponding to the set $\{(y, z) : |y| = \frac{\pi}{2}\ or\ |z| = \frac{\pi}{2}\}$ correspond to their stable and unstable manifolds.

On these faces, the velocity field Eq. (3) has only one component, and its flow simplifies since there, the modulus $k \to 1$, and $\mathrm{sn}(T, 1) = \tanh(T)$, and $\mathrm{cn}(T, 1) = \mathrm{dn}(T, 1) = \mathrm{sech}(T)$. In this case Eq. (9) becomes

$$\Phi_T(x, y, z) = \begin{cases} \left(x, y, \sin^{-1}\left(\frac{\cosh(T)\sin(z) \pm \sinh(T)}{\cosh(T) \pm \sin(z)\sinh(T)}\right)\right) , & \text{if } y = \pm\frac{\pi}{2} \\ \left(x, \sin^{-1}\left(\frac{\cosh(T)\sin(y) \mp \sinh(T)}{\cosh(T) \mp \sin(y)\sinh(T)}\right), z\right) , & \text{if } z = \pm\frac{\pi}{2} \ . \end{cases} \tag{23}$$

This formula for $T = T_1$ gives the the boundary map corresponding to F_1; we denote it as B_1. The maps B_2 and B_3 are obtained from Eq. (23) by permuting the variables appropriately.

It is convenient to use a spherical projection to display the dynamics of the system. Letting (θ, ψ) denote the longitude and colatitude, respectively, we can project the cube onto the sphere. Then the dynamics can be displayed on the rectangle $-\pi < \theta \leq \pi,\ 0 \leq \psi \leq \pi$. For example, in Fig. 6 we show F_1 and F_3 in this projection. In this figure, the twelve edges of the cube project to the red curves. The faces $x = \pm\frac{\pi}{2}$ are pierced in the center by the points $(\theta, \psi) = (0, \frac{\pi}{2})$ and $(\theta, \psi) = (\pi, \frac{\pi}{2})$ respectively. The faces defined by $z = \pm\frac{\pi}{2}$ correspond to those with ψ near 0 and π. The remaining panels define $y = \pm\frac{\pi}{2}$.

Now consider the two-roll composition

$$F_1 \circ F_3 \ .$$

Since the cube is an invariant surface for each map, it is still invariant. The eight vertices, $v_{\pm\pm\pm} = (\pm\pi/2, \pm\pi/2, \pm\pi/2)$, are saddle fixed-points. These points are represented by the intersections of the red curves in Fig. 6. The edges of the cube now comprise parts of the stable or unstable manifolds of the saddle fixed points.

On the two faces defined by $y = \pm\frac{\pi}{2}$, the boundary behavior is given by $B_1 \circ B_3$ because both of the moduli of the corresponding flows are one. Fig. 6 shows simple dynamics on this

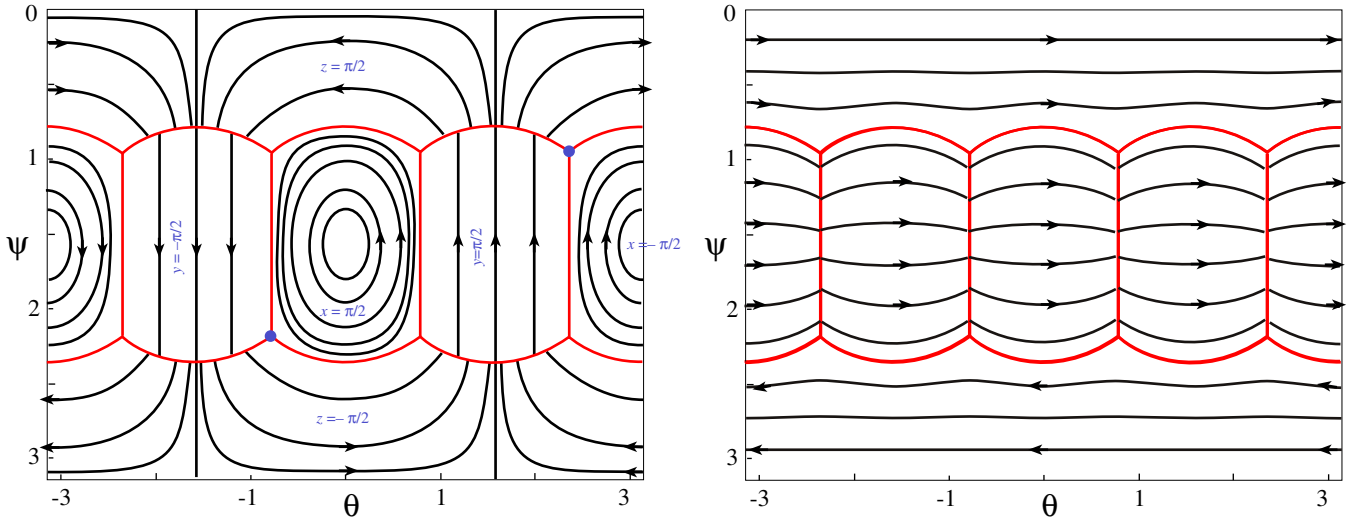

Figure 6: Maps on the boundary cube projected onto the spherical angles (θ, ψ). Invariant curves of F_1 are shown in the left panel and those of F_3 in the right.

face corresponding to shear flows. The face $y = \frac{\pi}{2}$ is a branch of the stable manifold of the saddle v_{-++} (shown as a blue dot in Fig. 6). Similarly, the boundary face $y = -\frac{\pi}{2}$ is a branch of the stable manifold of v_{+--}. The Jacobian at the vertices is easily evaluated by linearizing the flow at a saddle equilibrium to obtain $DF_1 = \mathrm{diag}(1, e^{s_1 T_1}, e^{-s_1 T_1})$, where $s_1 = \mathrm{sgn}(yz)$, and $DF_3 = \mathrm{diag}(e^{s_3 T_3}, e^{-s_3 T_3}, 1)$, where $s_3 = \mathrm{sgn}(xy)$. Thus at the vertex v_{-++}

$$DF_1 \circ DF_3 = \mathrm{diag}(e^{-T_3}, e^{T_1+T_3}, e^{-T_1}) \; . \tag{24}$$

On the four remaining faces, the dynamics is determined by either $F_1 \circ B_3$ or $B_1 \circ F_3$, and even these simplified maps can have complicated behavior. Here we will discuss the existence of fixed points. For example consider $F_1 \circ B_3$ on the face $x = \pi/2$. In the simplest case, when $T_3 = 0$, the dynamics is simply the sheared rotation defined by the single roll. The rotation number of F_1 is

$$\omega = \frac{T_1}{4K(k)}$$

where K is the complete elliptic integral, and k is the modulus Eq. (8). Since $K(0) = \frac{\pi}{2}$, ω starts at $\frac{T_1}{2\pi}$ at $(\frac{\pi}{2}, 0, 0)$, and decreases to zero at the edges; therefore there will be fixed points at the center of the face and on any streamline for which ω is an integer. If we restrict to $0 < T_1 < 2\pi$, there is exactly one elliptic fixed point on the face, the point $(\frac{\pi}{2}, 0, 0)$. Moreover, the implicit function theorem implies that this fixed point persists for T_3 nonzero, since the elliptic fixed points have eigenvalues not equal to 1.

Because B_3 is applied before F_1 and we are considering only rolls with positive rotation, all fixed points reside on the $y < 0$ half of the face $x = \frac{\pi}{2}$. Since the streamlines of F_1 are symmetric about the plane $y = 0$, and B_3 changes y only, any fixed point must occur on a line $y = -c$ such that $B_3(-c, z) = (c, z)$, and correspondingly, we must have $F_1(c, z) = (-c, z)$. The points $(\pm c, z)$ reside on the same streamline of F_1, and therefore there must be a T_1 such that $F_1(c, z) = (-c, z)$ (up to $4K$ periodicity) because the curves are continous, closed loops.

Indeed, for large enough values of T_1 there can be multiple fixed points on this face. To see this, consider the vertical line segments $l_\pm = \{(y = \pm c, z)\}$, see Fig. 7. For each c, there exists a T_3

such that $B_3(l_-) = l_+$. The image of l_+ under F_1 can be quite complex. As shown in the figure, if $T_1 < T_3$, $F_1(l_+)$ does not intersect l_-, and there are no fixed points on the face. For $T_1 = T_3$, $F_1(l_+)$ (the red curve) intersects l_- at $z = \frac{\pi}{2}$. When T_1 is slightly greater than T_3, we have at most one fixed point because there is only one intersection; however, if $T_1 >> T_3$ (the cyan curve), there can be many fixed points. If there is one intersection, then this point is actually a fixed point, as symmetry implies that $F_1(c, z) = (-c, z)$. However, if $F_1(l_+)$ intersects l_- in several places, not all intersections need have the same z coordinate after iteration. When there exist more than three such intersections, then some of them can be candidates for additional fixed points.

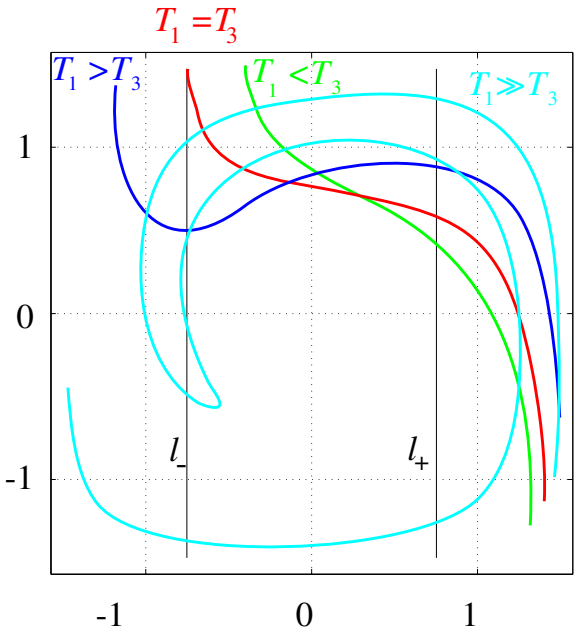

Figure 7: Fixed Points of $F_1 \circ B_3$ at $x = \frac{\pi}{2}$. Here $l_+ = B_3(l_-)$ and the colored curves are images of l_+ under F_1.

One can understand fixed points on the other faces by a similar argument.

7 Numerical Explorations

In this section we will explore some of the dynamics Eq. (6). For simplicity, we set $T_2 = 0$ so that the second roll is not active, giving the system

$$F = F_1 \circ F_3 \tag{25}$$

As we showed in §5, it is sufficient to consider to $T_1 > T_3 > 0$.

First we discuss the techniques that we will use to visualize the orbits of Eq. (25). We take advantage of the fact that orbits are constrained to surfaces of constant $J(x, y, z) = \cos(x)\cos(y)\cos(z)$, and that for each $0 < J \leq 1$ these surfaces are convex, topological spheres, recall Fig. 3. Therefore as we did in §6.2 for the maps on the boundary, we can use spherical coordinates to obtain a two-dimensional projection of the dynamics. Letting (θ, ψ) be the spherical angles, any point (x, y, z) corresponds to a point (J, θ, ψ), and since J is invariant, we can view the dynamics in the angle plane. The coordinate transformation is thus

$$(J, \theta, \psi) = V(x, y, z) = \left(\cos(x)\cos(y)\cos(z), \tan^{-1}\left(\frac{y}{x}\right), \tan^{-1}\left(\frac{\sqrt{x^2+y^2}}{z}\right)\right) , \tag{26}$$

which has the Jacobian

$$\det(DV) = J\frac{x\tan x + y\tan y + z\tan z}{\sqrt{x^2+y^2}(x^2+y^2+z^2)} \ . \tag{27}$$

To visualize the dynamics on the (θ,ψ) plane for a given invariant value, we will iterate a grid of initial conditions. For each (θ,ψ), we first determine the radius, r, using Newton method on $J(r\sin\psi\cos\theta, r\sin\psi\sin\theta, r\cos\psi)$, and then transform to Cartesian coordinates to obtain the initial point for Eq. (25). For subsequent iterates, we can simply project out the spherical radius and plot (θ,ψ) along the orbit. To view the dynamics in the entire cube, we choose a grid in J (from 1 to 0), and concatenate the figures to create an animation.[2] The animations reveal a system rich in complex, chaotic behavior.

Recall that when a map has an invariant, fixed points generically come in one-parameter families labelled by the invariant value [31]. Suppose that $\mathcal{O} = \{x_t, t = 0,\ldots,n-1\}$ is a periodic orbit of period n. Differentiating the equation $J(F^n(x)) = J(x)$ at the point x_0 gives

$$(DF^n(x_0))^T \cdot \nabla J(x_0) = \nabla J(x_0) \tag{28}$$

Thus when $\nabla J(x_0) \neq 0$ (as is true on all invariant surfaces except the origin and the fundamental cube), this vector is a left-eigenvector of the Jacobian with unit multiplier. Since F is volume-preserving this implies that the multipliers of $\mathcal{O}$ are $(1,\lambda,\frac{1}{\lambda})$. When $\lambda \neq 1$, the implicit function theorem can be used to show there is a curve of fixed points of F^n parameterized by J through x_0. When $\lambda \neq \pm 1$, the periodic orbit is elliptic on the invariant surface if λ is on the unit circle, and hyperbolic when λ is real. The orbit generically undergoes q-tupling bifurcations when λ passes through the value $e^{2\pi i\omega}$ with $\omega = p/q$ rational. These bifurcations correspond to the creation of new periodic orbits of period nq; these new orbits are also found in one-parameter families parameterized by J.

To compute some of the low period orbits we use Broyden's method [30]. For the fixed points, we allowed the initial guess for Broyden's method to range over the entire invariant surface, so that we had a good chance of finding all of them. However, to limit the complexity of the figures, we decided only to search for periodic points born at the q-tupling bifurcations of the fixed points. An analytic expression for the Jacobian can be computed to determine the stability of the periodic points.

The analysis of fixed and periodic points gives us the ability to understand the fine structure of the system. It also illuminates any barriers to global transport on each invariant. For instance, the existence of large islands surrounding stable periodic points inhibits the transport of passive scalars. On the other hand, the existence of hyperbolic periodic points should aid transport due to the likelihood of homoclinic and heteroclinic tangles in their manifolds.

One measure of the degree of chaos in a system are its Lyapunov exponents. Since F is volume-preserving, the sum of its three exponents must be zero, and because the orbits are restricted to 2D surfaces, one of the exponents must be exactly equal to zero. This implies that the remaining two exponents are equal in magnitude and opposite in sign. We use the iterative QR method to compute the exponents [37]. Along an orbit $\mathcal{O}$, define

$$Q^{(n+1)}\,R^{(n+1)} = DF(x_n)\,Q^{(n)}\,R^{(n)} \ ,$$

where $Q^{(0)} = R^{(0)} = id$. As usual Q is orthogonal and R is upper triangular. To compute the exponents, we require that $R_{ii} > 0$; it is not hard to show that one can modify the QR method so that this is the case. Moreover, since F is orientation preserving, and $\det(R) > 0$, then $Q \in SO(3)$.

[2] We attach several animations as movie files to this paper.

Thus we can represent Q with three angles, θ_i (for example Euler angles or rotations about three orthogonal axes). Since

$$R^{(n+1)}\,(R^{(n)})^{-1} = (Q^{(n+1)})^T\,DF(x_n)\,Q^{(n)}\ ,$$

is upper triangular, this requirement can be manipulated to provide a formula for updating the angles θ_i iteratively. After n steps, the i^{th} Lyapunov exponent is approximately

$$\lambda_i^{(n)} = \frac{\ln R_{ii}^{(n)}}{n}\ .$$

They can be computed iteratively using

$$\lambda_i^{(n)} = \frac{1}{n}\left((n-1)\lambda_i^{(n-1)} + \ln((Q^{(n)})^T\,DF(x_n)\,Q^{(n-1)})_{ii}\right)\ .$$

We compute the exponents on a (θ,ψ) grid of initial conditions on each invariant surface. In order to resolve islands from the chaotic sea, a very fine grid is used and a large number of iterations are performed to get reasonable accuracy in the exponent. For all animations, Fig. 11, Fig. 12, Fig. 15, and Fig. 16, 15000 iterations were performed on an 81×51 grid of initial conditions on each invariant surface.[3] We measure accuracy by averaging the standard deviation, $\langle\sigma\rangle$, of the final 1000 iterates over a given invariant via Eq. (29). As expected the accuracy depends strongly on the behavior in the phase plane. For the example given in §7.1, we find $\langle\sigma\rangle = .0001$ when $J = .1$ and $\langle\sigma\rangle = .0115$ when $J = .8$. Between these values, an increasing trend is noted as the behavior evolves from regular to increasingly chaotic. For Fig. 14 and Fig. 17, 15000 iterations were also performed on slightly smaller grids of size 81×41.

As an average measure of chaos on the invariant surface we compute the surface average of the positive Lyapunov exponent. The average of any function on a surface is approximated by

$$\langle f\rangle = \frac{1}{A}\sum_{i,j}^{n_\theta,n_\psi} f(x_{ij})\frac{|\nabla J(x_{ij})|\Delta\theta\Delta\psi}{|\det(DV(x_{ij})|}\ , \tag{29}$$

Here $|\nabla J|/|\det(DV)|$ is the surface area element with the Jacobian Eq. (27), A, the surface area, is determined so that $\langle 1\rangle = 1$, and x_{ij} is the ij^{th} point on the surface grid with spacing $\Delta\theta$ and $\Delta\psi$.

We expect the Lyapunov exponents will be very small near the origin, since the normal form analysis in §6.1 indicates that orbits near the origin lie on invariant circles. Similarly the Lyapunov exponents near the boundary cube will tend toward those on the boundary faces. Recall that the two of the boundary faces, $y = \pm\frac{\pi}{2}$, correspond to branches of the stable manifold of vertices. From Eq. (24), the Lyapunov exponents on these faces are $(-T_3, -T_1)$. However, on the four remaining faces, the dynamics are quite complex. We will see that the effect of the uniform faces is to decrease the Lyapunov exponents near the boundary.

7.1 Example 1: $T_1 + T_3 = 12$

We begin by exploring some of the dynamics of Eq. (25) for the case $T_1 = 7$, $T_3 = 5$. Recall that near the origin, the map is approximately a rotation about the axis v_3, where v_3 is the eigenvector of $DF(0)$ with eigenvalue one. In Fig. 8 we show a projection of the dynamics onto the (θ,ψ)

[3]For the animations, Fig. 12, and Fig. 16, 399 invariant values were used. The generation of the Lyapunov data took approximately 2 weeks to run on a Pentium 4 processor.

plane for J near one; since $J = 1$ at the origin, the portrait shown in the figure corresponds to a small sphere near the origin. Most of the orbits lie on invariant circles, as suggested by the normal form analysis in §6.1. The apparent change in topology of the circles in the figure is due only to nonalignment of the spherical projection with the rotation axis. Note that the reflection symmetry through the origin implies that the northern and southern hemispheres have conjugate dynamics.

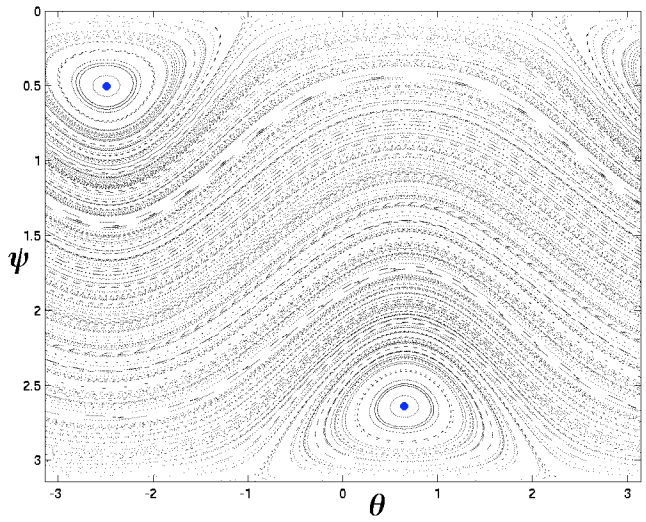

Figure 8: Projection of the dynamics of Eq. (25) onto the (θ, ψ) plane for $T_1 = 7, T_3 = 5$, on the invariant surface $J = 0.973962$.

There is a curve of fixed points tangent to the v_3 axis at the origin; this gives rise to a pair of fixed points on each invariant surface, and for these parameter values there are no other fixed points. We focus on the fixed point in the northern hemisphere—by symmetry the other fixed point has the same behavior. In Fig. 9, we plot the multipliers $(1, \lambda, \lambda^{-1})$ of this fixed point as a function of J. Note that $J = 1$ at top of the figure, corresponding to the origin in phase space, and J decreases to 0 at the base of the figure, corresponding to the bounding cube. Several q-tupling bifurcations are labeled in the figure. The phase space near several of these bifurcations is shown in Fig. 10. In this figure the four panels on the left show the tripling bifurcation near $J \approx .61$ (corresponding to the squares in Fig. 9). As is usual for area-preserving maps, there is a saddle-center bifurcation creating a pair of period-three orbits before the rotation number of the fixed point reaches $\frac{1}{3}$. The saddle then collides with the fixed point at the tripling and later reappears on the opposite side. The four panels on the right show a sequence of period 2 bifurcations near $J \approx .45$ (corresponding to the small bubble of instability in Fig. 9). The first doubling is supercritical, resulting in the creation of a stable period-two orbit (the fixed point becomes unstable). Subsequently at $J \approx .448465$, the unstable fixed point undergoes a subcritical doubling event thus spawning an unstable period-two orbit. At $J \approx .448222$, the unstable period-two orbit created from the previous split undergoes a pitchfork bifurcation thus creating a pair of unstable period-two orbits and a stable period-two orbit. When the sequence finishes, we have a stable fixed point, 2 stable period-two orbits and two unstable period-two orbits. There is a final supercritical doubling of the fixed point near $J = 0.27$, and for all smaller values of J, the fixed points are unstable.

In an attached QuickTime file,[4] we present an animation of the dynamics and maximal Lya-

[4]See http://amath.colorado.edu/studen/mullowne/example1.avi

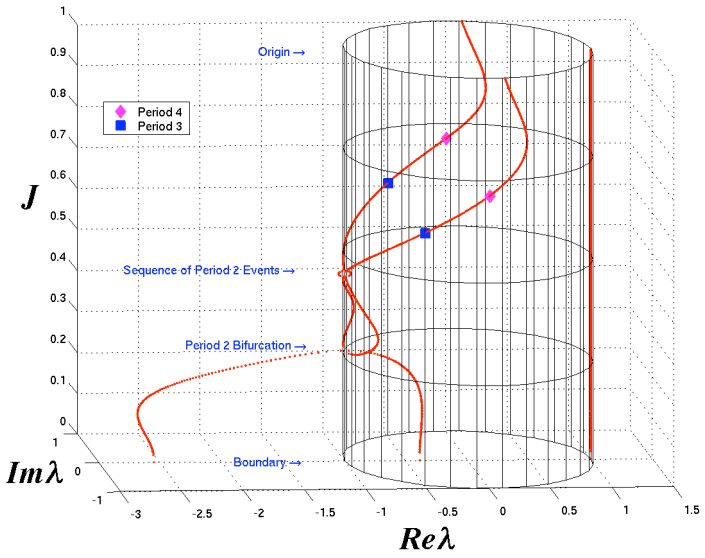

Figure 9: Multipliers of the fixed point of Eq. (25) as a function of J for $T_1 = 7$ and $T_3 = 5$. Doubling, tripling, and quadrupling bifurcations are noted.

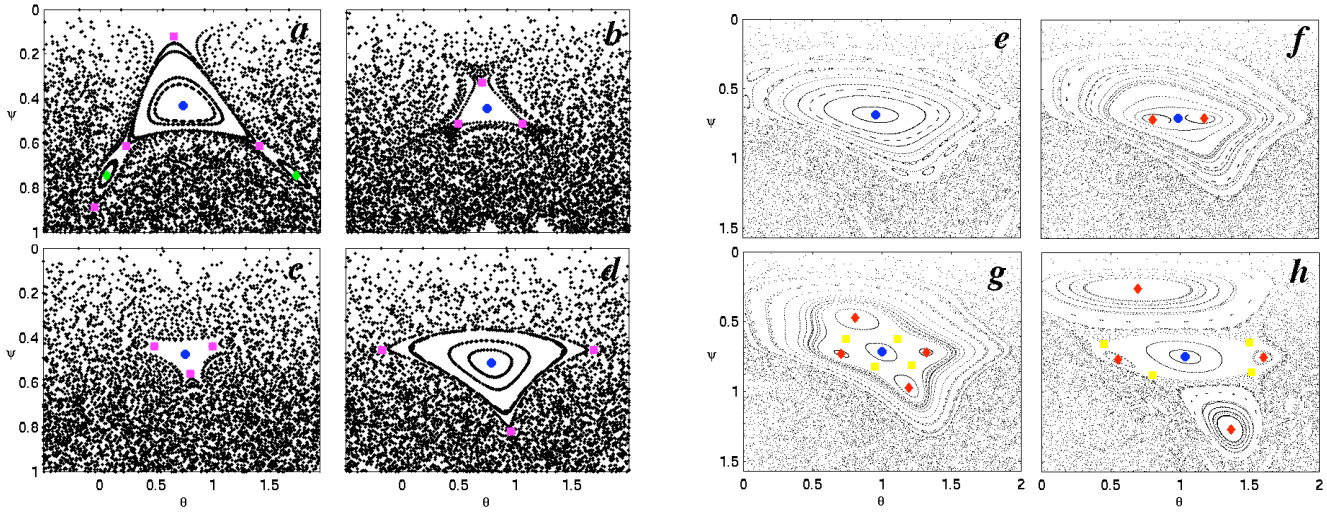

Figure 10: Tripling and doubling bifurcations of a fixed point for $T_1 = 7, T_3 = 5$. The fixed point is shown as the blue circle, the green diamond and purple square correspond to stable and unstable period three orbits, and the red diamond and yellow square are stable and unstable period two orbits. The four panels at the left correspond to (a) $J = 0.625940$, just after a saddle-center creating a pair of period three orbits, (b) $J = 0.618429$, just before tripling bifurcation, and (c) $J = 0.600902$ and (d) $J = 0.578368$ after the tripling. The right panels correspond to (e) $J = 0.465699$, and (f) $J = 0.450677$, just before and after the first, supercritical doubling, and (c) $J = 0.445669$, and (d) $J = 0.428143$, after the second, subcritical doubling and pitchfork bifurcations.

punov exponent for these parameter values. The movie consists of 399 frames starting at $J = .999$, and decreasing to $J = 0.002504$. For the dynamics panel, each initial condition on the grid of 18×18 points is iterated 300 times.[5] Also shown in the movie are panels that display the position of the fixed point in space, and its multipliers in the complex plane. A snapshot of the animation is shown in Fig. 11. The computations show a clear correspondence between the existence of island structures and small Lyapunov exponents. Outside of the islands, the Lyapunov exponent is nearly constant; however, there are several intervals of J where invariant circles far from the fixed points reappear (they are mostly destroyed for $J < 0.75$) and this causes a local reduction in the chaos. In general as J decreases, the dynamics become more chaotic, though as J nears zero the influence of the boundary dynamics appears in the animation by a concentration of chaotic motion near the edges of the cube and the reappearance of islands that correspond to stable fixed points on the boundary.

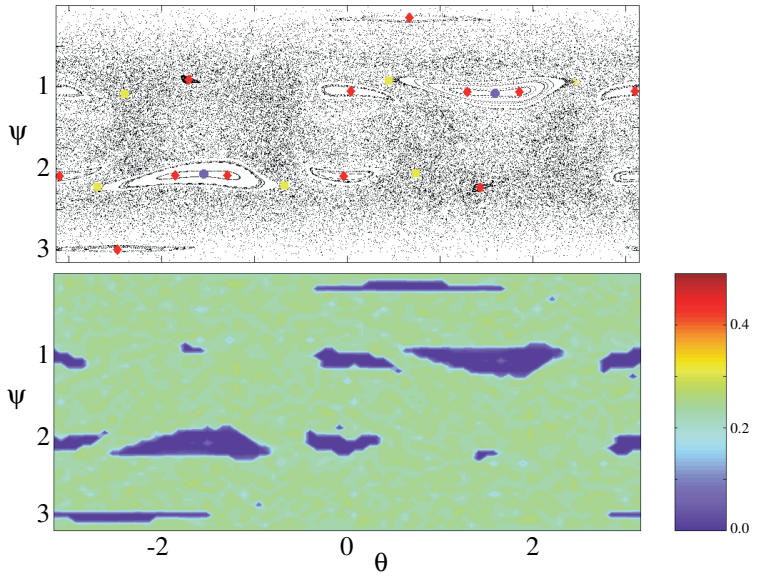

Figure 11: Phase Plane and the Lyapunov exponent for $J = 0.262895$. Points in the phase plane (upper panel) correspond to periodic orbits; colors are the same as Fig. 10. The bottom panel shows the largest Lyapunov exponent for a grid of initial conditions.

In Fig. 12 we show the scaled surface average of the largest Lyapunov exponent, $\frac{\langle\lambda\rangle}{T}$ (where $T = T_1 + T_3$), as a function of J using Eq. (29). Prominent bifurcations and characteristics of the phase portrait are indicated on the figure. The scaled average Lyapunov exponent remains nearly zero as J decreases from 1, until near $J = 0.8$, when $\frac{\langle\lambda\rangle}{T}$ suddenly begins to increase. This suggests that the asymptotic validity of the normal form breaks down near this point, and corresponds with the appearance of small zones of chaotic behavior. At the quadrupling and tripling bifurcations, $\frac{\langle\lambda\rangle}{T}$ reaches local maxima, and two local minima are associated with prominent period-two islands. The global maximum of $\frac{\langle\lambda\rangle}{T}$ occurs just inside the boundary, after which a steep decrease occurs. As we saw in §6.2, this is to be expected because the Lyapunov exponents are negative on two of the six boundary faces.

[5]Note the movie doesn't quite start and end at $J = 1$ and 0. $J = 1$ corresponds to the lone fixed point at the origin thus we omitted this frame. For $J = 0$, the Lyapunov code exhibited extreme sensitivity which couldn't be resolved easily.

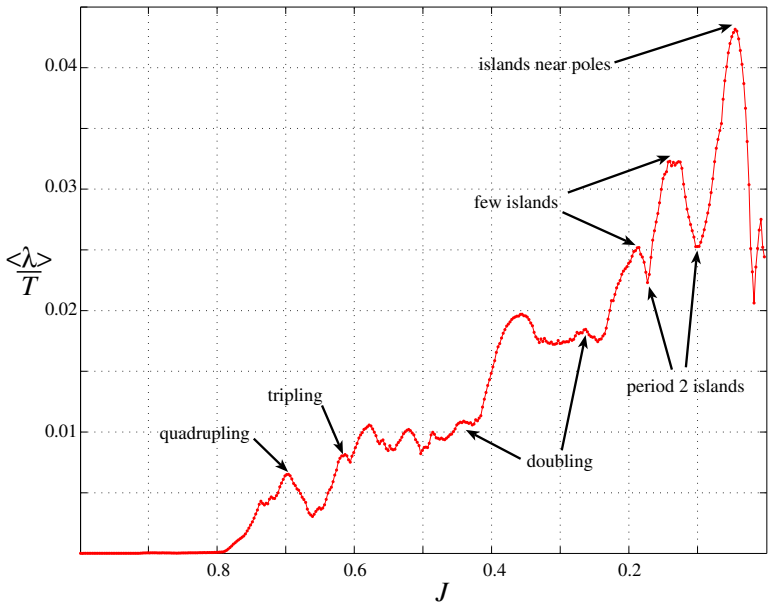

Figure 12: Average scaled maximal Lyapunov Exponent for $T_1 = 7$, $T_3 = 5$.

Though three-dimensional mixing is forbidden by the existence of the invariant, mixing does occur on the invariant surfaces. To visualize this, we start a group of points in a small region, see Fig. 13, and view them at successive times. Results of these computations reinforce the conclusion that limited transport occurs near the origin, but that as J decreases, mixing occurs on increasing scales and more rapidly. This mixing, however, is not complete, as islands can be seen in the panels even with the smallest values of J.

To explore the dependence of the Lyapunov exponents on the choice of parameters, we now fix $T_1 + T_3 = 12$, and vary the times in Fig. 14. For each panel in the figure, $\frac{\langle\lambda\rangle}{T}$ is plotted as a function of T_3 for a fixed J. Note that each figure is symmetric about the point $T_1 = T_3$, as predicted by the symmetry analysis in §5. This figure shows that there is no choice of T_3 such that $\frac{\langle\lambda\rangle}{T}$ is maximized on every invariant surface; however, there are large values of $\frac{\langle\lambda\rangle}{T}$ for most J when $T_3 \approx 2$ or 10. This case might be expected to have the largest two-dimensional mixing on the surfaces of constant J.

The dynamics on the cubical boundary for this case are relatively uninteresting. The advection is so strong that the vast majority of iterates get pushed to the vertices or edges almost immediately.

7.2 Example 2: $T_1 + T_3 = 6$

In this section we fix the total time to $T_1 + T_3 = 6$, half of the previous value. We will first consider the case $T_1 = 3.5$ and $T_3 = 2.5$, and see that the dynamics on the boundary has an influence that extends far into the interior of the cube.

We observe that for this case, as in §7.1, there is a single curve of fixed points that emanates from the origin. The fixed points also have a bubble of instability that begins with a supercritical doubling near $J \approx 0.92$. Two new pairs of period-two orbits are born in saddle-center bifurcations near the poles when $J \approx 0.8$, and the new stable period-two orbits collide with the fixed points in a subcritical doubling at $J \approx 0.77$, completing the bubble. Unlike the previous case, the fixed points do not undergo another doubling bifurcation after they regain stability as J continues to decrease;

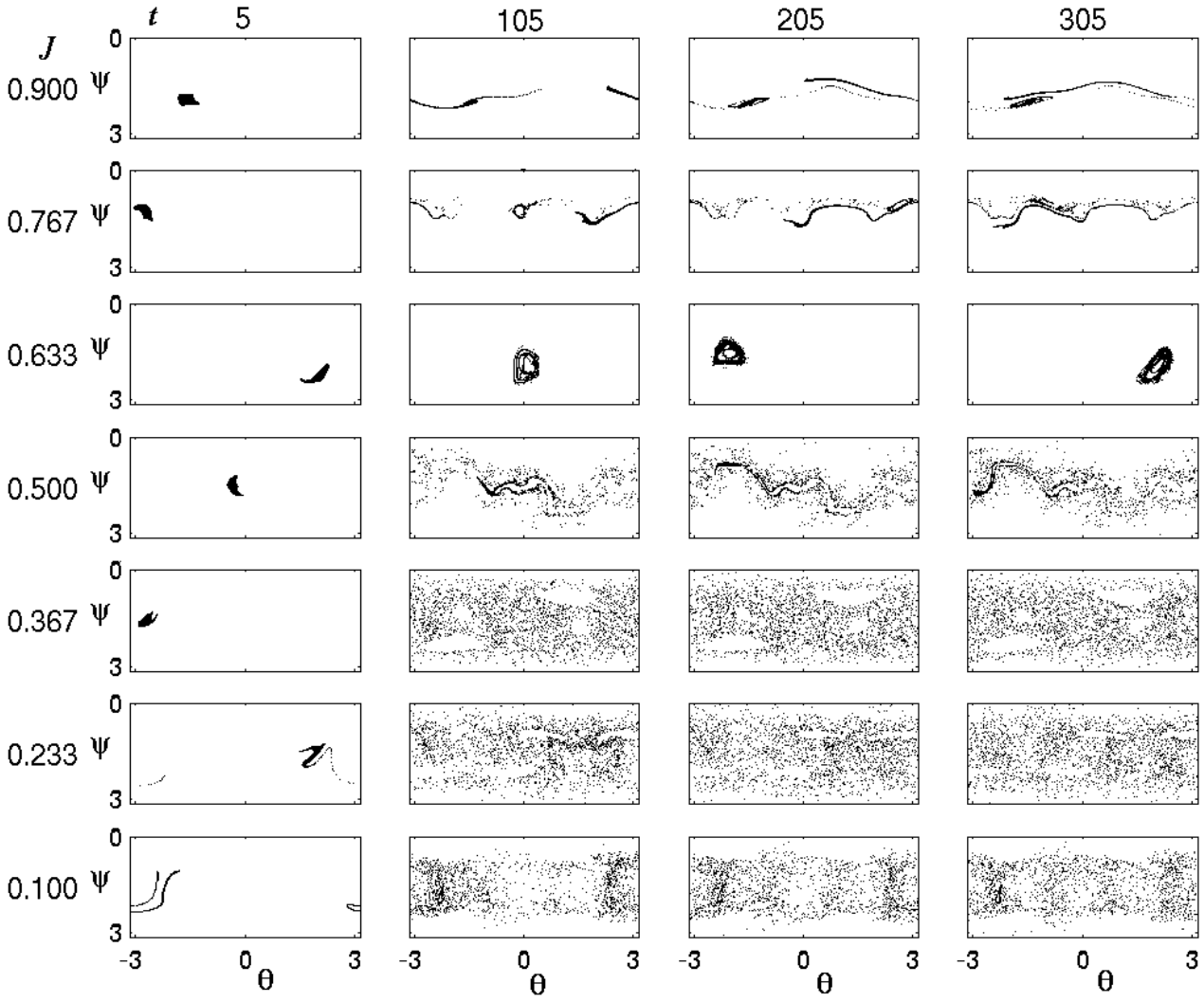

Figure 13: Local mixing for $T_1 = 7$, $T_3 = 5$. Here a 45×45 grid of points is started in the region $-\frac{\pi}{20} \leq \theta \leq \frac{\pi}{20}$ and $\frac{9\pi}{20} \leq \psi \leq \frac{11\pi}{20}$. The rows correspond to different surfaces of constant J, and the columns to increasing numbers of iterates.

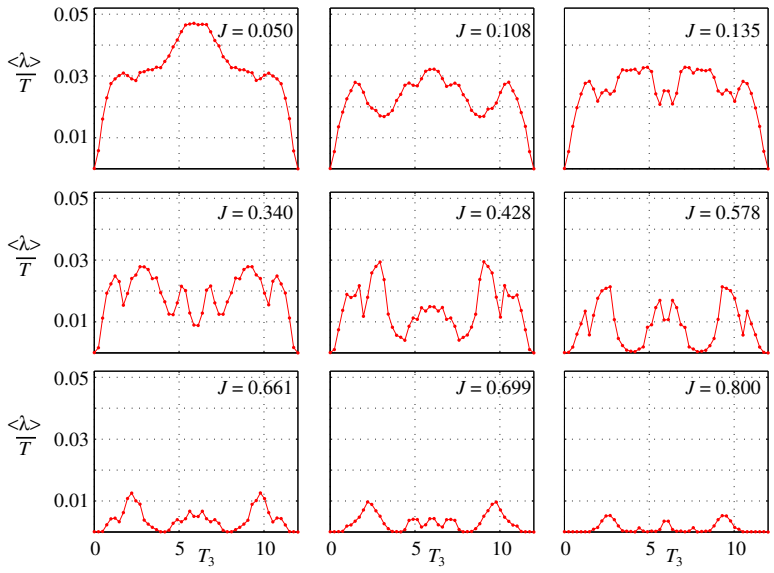

Figure 14: Average Lyapunov Exponent for varying T_3 with $T_1 + T_3 = 12$.

instead they remain stable (apart from a momentary instability at several tripling bifurcations) [6] to $J = 0$. These fixed points continue to those on the boundary faces $x = \pm\frac{\pi}{2}$.

In Fig. 15 we show two panels from an animation for this case.[7] In the left panel, where $J = 0.282925$, there are large period-three islands surrounding the fixed point—these were born in a saddle-center bifurcation at $J \approx 0.306$. Islands from an earlier five-tupling bifurcation are also prominent (one of these islands encloses the pole, and is thus hard to see in the projection). A band of regular behavior corresponding to invariant circles separates the surface into two invariant hemispheres; these have conjugate dynamics under the reflection symmetry R in Eq. (15).

The right panel of Fig. 15 shows the case $J = 0.030045$, close to the bounding cube. In this case there is an even larger band of meandering, invariant circles, and a corresponding region of the small Lyapunov exponents. The boundary dynamics (recall Fig. 6) strongly influences the dynamics on this surface. In the regions that correspond to the faces $y = \pm\frac{\pi}{2}$, the dominant motion sweeps the trajectories across the face, and helps give rise to the invariant circles. Near the faces $x = \pm\frac{\pi}{2}$, the dynamics is predominantly chaotic, with the exception of small elliptic islands around the sole fixed point on each face.

In Fig. 16 we show the average Lyapunov exponent as a function of J. As in Fig. 12, $\frac{\langle\lambda\rangle}{T} \approx 0$ for an initial interval near the origin; however, now $\frac{\langle\lambda\rangle}{T}$ increases more or less monotonically, until $J \approx 0.22$, when it plunges rapidly to a local a minima at $J \approx 0.14$. This plunge occurs when the fixed points have multipliers that hover near the tripling point, and seems to be associated with the creation of many modest size elliptic regions in the phase space. Note that the overall magnitude of $\frac{\langle\lambda\rangle}{T}$ is similar in this case to the previous one up until $J \approx .22$.

Finally we show $\langle\lambda\rangle$ as a function of T_3 for $T_1 + T_3 = 6$ in Fig. 17. Once again, there seems to be no consistent choice of T_1 and T_3 such that $\frac{\langle\lambda\rangle}{T}$ is maximized over every invariant. It is interesting to note however that near the origin, $\frac{\langle\lambda\rangle}{T}$ is maximized for equal times, in contrast with the results in Fig. 14. However as before, the largest Lyapunov exponents on most surfaces seem

[6] It would be nice to find these. How many are there? where? The eigenvalues in the movie seem to interestingly hover around $2\pi/3$.

[7] See the attached file at http://amath.colorado.edu/student/mullowne/example2.avi

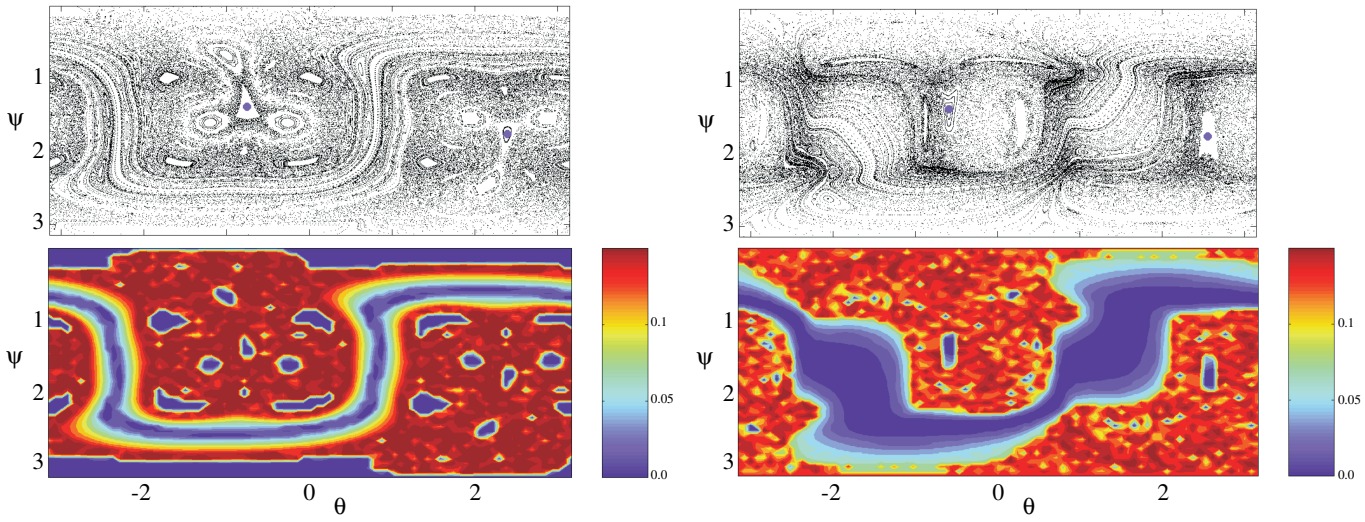

Figure 15: Dynamics for $T_1 = 3.5$, $T_3 = 2.5$. The left panels correspond to $J = 0.282925$, and the right to $J = 0.030045$.

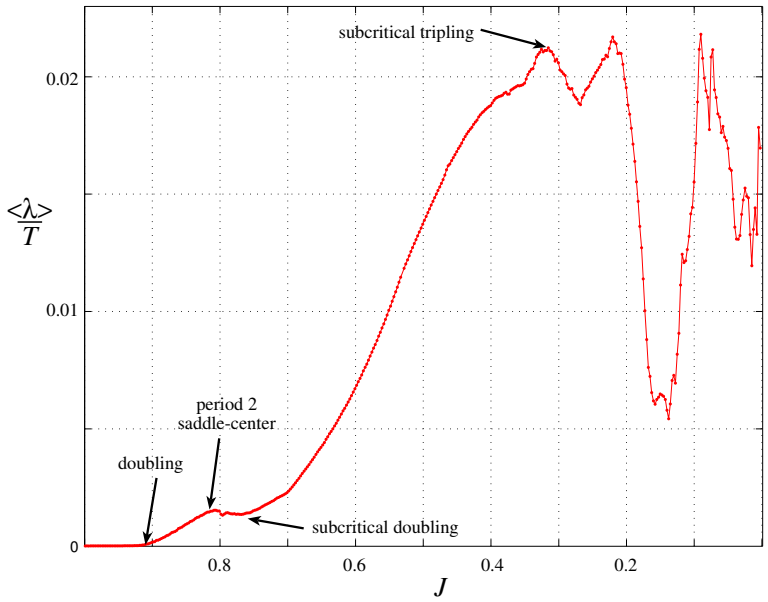

Figure 16: Surface average of the maximal Lyapunov exponent as a function of J for $T_1 = 3.5$, $T_3 = 2.5$.

to occur when the time parameters substantially differ, in this case for $T_3 = 1.5$ or 4.5.

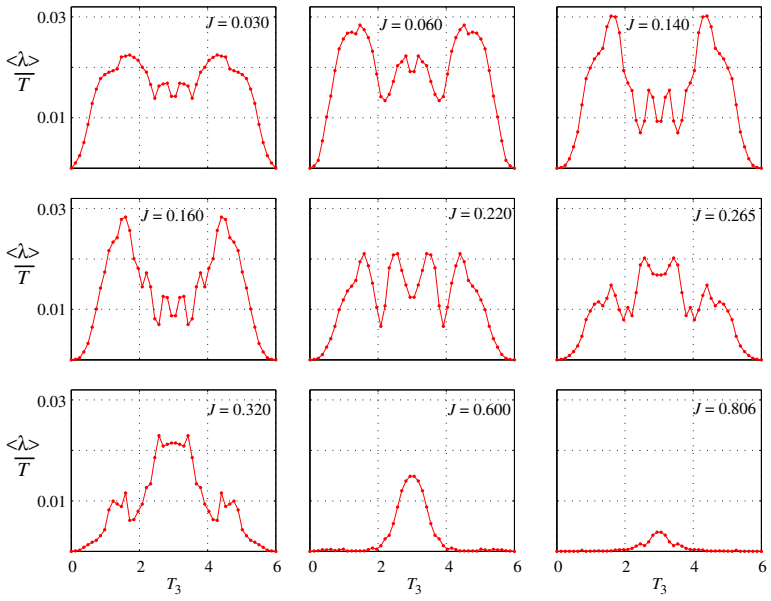

Figure 17: Average Lyapunov Exponent vs Time, Fixed Invariants.

8 Conclusions

In 1984, Aref outlined a general, mathematically tractable stirring protocol for passive tracers chaotically advected by point vortices with specified location, strength and lifetime. We have presented a simple, three-dimensional, incompressible flow analogous to Aref's two-dimensional blinking vortex model. In its most general form our model consists of a superposition of nonautonomous two-dimensional roll arrays. It simplifies considerably if the rolls act sequentially and are turned on and off instantaneously; for in this case, each two-dimensional flow lies on streamlines of the corresponding stream function. We have studied the case of orthogonal roll arrays with identical aspect ratio in detail, where the two-dimensional flow can be obtained analytically in terms of elliptic functions.

For this case there is an invariant J, Eq. (14), so that the motion is confined to topological spheres. Nevertheless, the dynamics on each two-dimensional surface can exhibit all of the complexity of area-preserving mappings. We have shown that the dynamics near the intersection of the centers of the rolls lies on families of invariant circles and can be described by an asymptotic normal form. The corresponding phase portraits show no chaos in this regime. The motion is constrained by the outermost boundary, which for our system is an invariant cube. Each face of the cube is invariant, and several of the faces have simpler dynamics corresponding to laminar shear and/or laminar shear followed by rotation. The onset of chaos occurs suddenly some distance from the origin, and, as measured by Lyapunov exponents, exhibits irregular growth as we continue to move way from the origin that is associated with bifurcations of fixed points and low period orbits.

In order to achieve true three-dimensional mixing in systems composed of roll arrays, the invariant must be broken. In [38], roll arrays of identical aspect ratio and axes ($\hat{\mathbf{e}}_2$ and $\hat{\mathbf{e}}_3$) were positioned such that their respective intersections with $\hat{\mathbf{e}}_1$ were 90° out of phase. Their investigations showed local and global three-dimensional mixing. Other possible constructions that may

achieve three-dimensional mixing include (non)orthogonal roll arrays with identical/different aspect ratios. In the case of nearly orthogonal alternating roll arrays with identical aspect ratio, our preliminary investigations have shown that the invariant is in fact destroyed by this kind of perturbation. Initial studies indicate that the mixing near the intersection of roll axes is strongly influenced by the former invariant surfaces. This case also allows for transport between adjacent rolls. This case is unusual in a perturbation sense, since the unperturbed flow is chaotic itself. In the idealized limit where we consider infinite roll arrays, studies of transport throughout the domain can be understood under the framework of anomalous diffusion theory [39, 40, 41, 42]. In a construction analogous to the Küppers-Lortz phenomenon, roll arrays rotating by 60° also display three-dimensional mixing. We will report on these topics in a future paper.

References

[1] J.M. Ottino. *The Kinematics of Mixing: Stretching, Chaos, and Transport*. Cambridge Univ. Press, Cambridge, 1989.

[2] A.D. Stroock, S.K.W. Dertinger, A. Ajdari, I. Mezic, H.A. Stone, and G.M. Whitesides. Chaotic mixer for microchannels. *Science*, 295:647–651, 2002.

[3] M.G. Brown and K.B. Smith. Ocean stirring and chaotic low-order dynamics. *Physics of Fluids*, 3:1186–1192, 1991.

[4] C.K.R.T. Jones and S. Winkler. Invariant manifolds and Lagrangian dynamics in the ocean and atmosphere. *Handbook of Dynamical Systems, Vol. 2*, pages 55–92, 2002.

[5] G. Metcalfe, T. Shinbrot, J.J. McCarthy, and J. M. Ottino. Avalanche mixing of granular solids. *Nature*, 374(March 2):39–41, 1995.

[6] C. Lopez, E. Hernandez-Garcia, O. Piro, A. Vulpiani, and E. Zambianchi. Population dynamics advected by chaotic flows: A discrete-time map approach. *Chaos*, 11(2):397–403, 2001.

[7] I. Scheuring, G. Karolyi, Z. Toroczkai, T. Tel, and A. Pentek. Competing populations in flows with chaotic mixing. *Theoretical Populational Biology*, 63(2):77–90, 2003.

[8] Z. Neufield, P.H. Haynes, and T. Tel. Chaotic mixing induced transitions in reaction-diffusion systems. *Chaos*, 12(2):426–438, 2002.

[9] H. Aref. The development of chaotic advection. *Physics of Fluids*, 14:1315–1325, 2002.

[10] T. Dombre, U. Frisch, J.M. Greene, M. Hénon, A. Mehr, and A.M. Soward. Chaotic streamlines in the ABC flows. *J. Fluid Mech*, 167:353–391, 1986.

[11] H. Aref. Stirring by chaotic advection. *Journal of Fluid Mechanics*, 143:1–21, 1984.

[12] E. Moses and V. Steinberg. Stationary convection in a binary mixture. *Physical Review A*, 43(2):707–722, 1991.

[13] G. Küppers and D. Lortz. Transition from laminar convection to thermal turbulence in a rotating fluid layer. *Journal of Fluid Mechanics*, 35(3):609–620, 1969.

[14] F.H. Busse and Heikes K.E. Convection in a rotating layer - simple case of turbulence. *Science*, 208:173–175, 1980.

[15] Y. Tu and M.C. Cross. Chaotic domain structure in rotating convection. *Physical Review Letters*, 69(17):2515–2518, 1992.

[16] Y. Hu, W. Pesch, G. Ahlers, and R.E. Ecke. Convection under rotation for Prandtl numbers near 1: Kuppers-Lortz instability. *Physical Review E*, 58(5):5821–5833, 1998.

[17] R. Toral, M. San Miguel, and R. Gallego. Period stabilization in the Busse-Heikes model of the Küppers-Lortz instability. *Physica A*, 280:315–336, 2000.

[18] O. Piro and M. Feingold. Diffusion in three-dimensional Liouvillian maps. *Physical Review Letters*, 61:1799, 1988.

[19] M. Feingold, L.P. Kadanoff, and O. Piro. Passive scalars, three-dimensional volume-preserving maps, and chaos. *Journal of Statistical Physics*, 50(3-4):529–565, 1988.

[20] J. H. E. Cartwright, M. O. Feingold, and O. Piro. Passive scalars and three-dimensional Liouvillian maps. *Physica D*, 76:22–33, 1994.

[21] J.H.E. Cartwright, M. Feingold, and O. Piro. Chaotic advection in three dimensional unsteady incompressible laminar flow. *Journal of Fluid Mechanics*, 316:259–284, 1996.

[22] L.P. Rom-Kedar, V.and Kadanoff, E.S. Ching, and C. Amick. The break-up of a heteroclinic connection in a volume preserving mapping. *Physica D*, 62(1-4):51–65, 1993.

[23] H.E. Lomelí and J.D. Meiss. Quadratic volume-preserving maps. *Nonlinearity*, 11:557–574, 1998.

[24] H.E. Lomelí and J.D. Meiss. Heteroclinic primary intersections and codimension one Melnikov method for volume-preserving maps. *Chaos*, 10(1):109–121, 2000.

[25] H. E. Lomelí and J.D. Meiss. Heteroclinic orbits between invariant circles in volume-preserving mappings. *Nonlinearity*, 16:1573–1595, 2003.

[26] T. Shinbrot, M.M. Alvarez, J.M. Zalc, and F.J. Muzzio. Attraction of minure particles to invariant regions of volume preserving flows by transients. *Physical Review Letters*, 86(7):1207–1210, 2001.

[27] G.O. Fountain, F.V. Khakhar, and J.M. Ottino. Visualization of three-dimensional chaos. *Science*, 281(31 July):683–686, 1998.

[28] G. O. Fountain, D. V. Khakhar, I. Mezic, and J.M. Ottino. Chaotic mixing in a bounded three-dimensional flow. *Journal of Fluid Mechanics*, 417:265–301, 2000.

[29] P. F. Byrd and M. D. Friedman. *Handbook of Elliptic Integrals for Engineers and Physicists.* Springer Verlag, 1954.

[30] B. P. Flannery, W. H. Press, S. A. Teukolsky, and W. T. Vetterling. *Numerical Recipes in C, The Art of Scientific Computing.* Cambridge University Press, 2nd edition, 1992.

[31] A. Gomez and J.D. Meiss. Volume-preserving maps with an invariant. *Chaos*, 12:289–299, 2002.

[32] P. Boyland. personal communication, May 2003.

[33] D.K. Arrowsmith and C.M. Place. *An Introduction to Dynamical Systems*. Cambridge University Press, Cambridge, 1990.

[34] G.D. Birkhoff. Surface transformations and their dynamical applications. *Acta Math.*, 43:1–119, 1920.

[35] A. Bazzani. Normal form theory for volume-preserving maps. *Z. Angew. Math. Phys.*, 44(1):147–172, 1993.

[36] A. Bazzani and A. Di Sebastiano. Perturbation theory for volume-preserving maps: application to the magnetic field lines in plasma physics. In *Analysis and modelling of discrete dynamical systems*, volume 1 of *Adv. Discrete Math. Appl.*, pages 283–300. Gordon and Breach,, Amsterdam, 1998.

[37] S. Habib, T.M. Janaki, G. Rangarajan, and R. D. Ryne. Computation of the Lyapunov spectrum for continuous-time dynamical systems and discrete maps. *Physical Review E*, 60(6):6614–6626, 1999.

[38] M.A. Fogleman, M.J. Fawcett, and T.H. Solomon. Lagrangian chaos and correlated Lévy flights in a non-Beltrami flow: Transient versus long-term transport. *Physical Review E*, 63:1–4, 2001. 020101.

[39] J. Klafter, A. Blumen, and M.F. Shlesinger. Stochastic pathway to anomalous diffusion. *Physical Review A*, 35(7):3081–3085, 1987.

[40] J. Klafter, G. Zumofen, M.F. Shlesinger, and A. Blumen. Scale invariance in anomalous diffusion. *Philosophical Magazine B*, 65(4):755–765, 1992.

[41] J. Klafter, G. Zumofen, and M.F. Shlesinger. Anomalous diffusion and Lévy statistics in intermittent chaotic systems. *Lecture Notes in Physics*, 457:183–210, 1995.

[42] J. Klafter, M.F. Shlesinger, and G. Zumofen. Beyond Brownian motion. *Physics Today*, pages 33–39, February 1996.